



RESEARCH ARTICLE

10.1029/2018JB016906

Experimental Study of Dislocation Damping Using a Rock Analogue

Key Points:

- The dominant deformation mechanism of borneol changes from diffusion to dislocation creep at about 2 MPa
- The attenuation spectra of a deformed sample display a high-frequency peak superposed on a high-temperature background
- The strain-induced microstructure and anelastic response demonstrate the potential importance of dislocations

Supporting Information:

- Supporting Information S1

Correspondence to:

Y. Takei,
ytakei@eri.u-tokyo.ac.jp

Citation:

Sasaki, Y., Takei, Y., McCarthy, C., & Rudge, J. F. (2019). Experimental study of dislocation damping using a rock analogue. *Journal of Geophysical Research: Solid Earth*, 124, 6523–6541. <https://doi.org/10.1029/2018JB016906>

Received 18 OCT 2018

Accepted 21 MAY 2019

Accepted article online 30 MAY 2019

Published online 25 JUL 2019

Yuto Sasaki¹ , Yasuko Takei¹ , Christine McCarthy² , and John F. Rudge³

¹Earthquake Research Institute, University of Tokyo, Tokyo, Japan, ²Lamont-Doherty Earth Observatory, Columbia University, Palisades, NY, USA, ³Bullard Laboratories, Department of Earth Sciences, University of Cambridge, Cambridge, UK

Abstract In order to explore the effects of dislocations on seismic velocity and attenuation, we conducted a series of forced oscillation and ultrasonic tests on rock analogue samples (polycrystalline borneol) that were predeformed under various differential stress $\Delta\sigma$. Additionally, creep experiments were conducted to determine the steady-state flow law for borneol. The dominant deformation mechanism of polycrystalline borneol changes from diffusion to dislocation creep at about $\Delta\sigma = 2$ MPa. At high stresses, power law creep with a stress exponent of ~ 4 was measured. Microstructure of the deformed samples showed wavy grain boundaries due to dislocation-induced migration and the occasional existence of microcracks. A borneol sample deformed in the dislocation creep regime showed a significant reduction in Young's modulus E and a slight increase in attenuation Q^{-1} at frequencies lower than 100 Hz, whereas E at ultrasonic frequency (10^6 Hz) did not reduce. Therefore, a major part of the dislocation creep-induced anelastic relaxation is a peak with a characteristic frequency between 100 and 10^6 Hz, which is much higher than the range of grain boundary-induced anelasticity of this material. Further experiments under higher confining pressure are needed to assess the relative contribution from dislocations and microcracks to this peak.

1. Introduction

Dislocations are linear defects, whose mobility (glide and climb) through the crystalline lattice facilitates shear deformation. Although dislocation density is considered to be controlled by the magnitude of long-term background stress (Kohlstedt & Goetze, 1974), the stress magnitude in the Earth's interior is subject to large uncertainty. Dislocations and dislocation-related microstructures, such as subgrain boundaries, are commonly observed in mantle nodules (e.g., Toriumi & Karato, 1978). Hence, dislocations as well as grain boundaries are considered to be pervasive in the mantle. Seismic waves propagating through these rocks drive dislocation motion and grain boundary sliding, causing dispersion and attenuation of the waves (rock anelasticity; e.g., Karato & Spetzler, 1990). Understanding of rock anelasticity is necessary to interpret the seismological structures in the Earth. Although significant progress has been made in the understanding of anelasticity associated with grain boundary sliding (Cooper, 2002; Gribb & Cooper, 1998; Jackson et al., 2002, 2004, 2014; Jackson & Faul, 2010; McCarthy et al., 2011; Morris & Jackson, 2009; Raj, 1975; Takei et al., 2014; Yamauchi & Takei, 2016), the effects of dislocations on rock anelasticity are poorly understood. Two preliminary studies explored the influence of dislocations on attenuation with olivine samples that were predeformed in dislocation creep (Farla et al., 2012; Guéguen et al., 1989). Although these studies demonstrated a clear dependence of attenuation on dislocation density, a comprehensive understanding of the mechanisms, needed for a seismological application, is lacking.

Anelasticity measurements using a forsterite single crystal (Guéguen et al., 1989) or olivine aggregates (Farla et al., 2012) are difficult because of the high temperature and/or high confining pressure needed to measure the anelastic relaxations active in the mantle. In studying anelasticity caused by grain boundary mechanisms, analogue experiments using organic polycrystals (high-purity borneol and borneol+diphenylamine binary eutectic system), which have a low melting temperature, have been playing an important role by providing well-constrained data over a broad frequency range (McCarthy et al., 2011; McCarthy & Takei, 2011; Takei et al., 2014; Yamauchi & Takei, 2016). In this study, by using the same analogue material (high-purity borneol) as these previous studies, we performed a series of experiments to investigate the effects of dislocations on anelasticity. Because the effects of grain boundary mechanisms on the anelastic properties of this

©2019. The Authors.

This is an open access article under the terms of the Creative Commons Attribution-NonCommercial-NoDerivs License, which permits use and distribution in any medium, provided the original work is properly cited, the use is non-commercial and no modifications or adaptations are made.

Table 1
High-Purity Borneol Samples Used in This Study

Sample no. (Geometry) ^a	Density (10 ³ kg/m ³)	Porosity ^b (%)	Grain size ^c <i>d</i> (μm)	Mechanical tests ^d	Final strain ^e ϵ_{fin}	Barrel distortion ^f
#120 (B)	1.006	0.5	15.3	Creep (40 °C)	0.10	0.004
#124 (B)	1.006	0.5	14.9 ^g	Creep (40 °C)	0.45	0.07
#121 (B)	1.007	0.4	—	Creep (50 °C)	0.36	0.01
#121A (A)	1.002	0.9	24.1 ^g	Creep (50 °C) without <i>P</i>	0.09	—
#122 (C)	1.005	0.6	16.2	Creep and forced oscillation	0.16	0.01
#123 (B)	1.007	0.4	16.6	Creep and ultrasonic	0.21	0.008
#127 (B)	1.008	0.3	17.7	Creep and ultrasonic	0.13	0.004

^aDiameter $2R$ (mm) and length L (mm) are, respectively, 15 and 13 for A, 30 and 30 for B, and 30 and 65 for C. ^bCalculated from the sample density relative to the density of borneol, 1.011×10^3 kg/m³. ^cGrain size was not measured when deformed microstructure was far from equilibrium. ^dEach type of test (creep, forced oscillation, and ultrasonic) was performed using a different apparatus. ^eCalculated as $(L_i - L_f)/L_i$ from the initial (L_i) and final (L_f) sample lengths. ^fCalculated as $(2D_m - D_t - D_b)/(D_t + D_b)$ from the top (D_t), middle (D_m), and bottom (D_b) diameter. ^gBefore deformation.

analogue material are well known, the effects of dislocations can be detected as a deviation from the grain boundary effects.

Borneol is designated a “plastic organic crystal,” which is considered to undergo ductile deformation by the same kinds of dislocation and diffusion processes as minerals, metals, and ceramics (Sherwood, 1979). However, a deformation mechanism map of borneol was not available and, hence, had to be determined in this study. In the following sections, we first report an experiment newly conducted to investigate the flow law of borneol, which clarifies the stress condition required for dislocation creep and which enabled us to investigate the effects of dislocations on the anelastic properties of a borneol polycrystal.

2. Experimental Details

2.1. Sample Fabrication

Samples and testing conditions used in this study are summarized in Table 1. Polycrystalline aggregates of organic borneol ($C_{10}H_{18}O$, melting temperature = 204.5 °C, D’Ans et al., 1964; Takei, 2000) were prepared following the procedure in Takei et al. (2014). Fine powder (~ 3 μm) of high-purity borneol, prepared from a cold-ball milling (−40 °C, 6 days), was placed in a cylindrical die and pressed to 13.9 MPa at room temperature for 4 days to produce fully dense, polycrystalline right circular cylinders (diameter $2R$, length L). Then, isothermal annealing was performed at about 3 MPa and 60 °C for 8 days, so that grain growth during the mechanical experiments in the following sections was negligible. (Sample #120 was annealed at about 3 MPa and 50 °C for 5 days.) After annealing, the sample was removed from the die. The initial sample geometry and mass were measured accurately and were used to calculate the initial sample density and porosity. The samples were almost transparent, consistent with small porosity (supporting information Figure S1). Further details of the sample preparation are presented in Takei et al. (2014).

The equilibrium microstructure of the as-fabricated polycrystalline aggregates of high-purity borneol is known from previous studies (McCarthy et al., 2011; Takei et al., 2014). Therefore, in this study, microstructure was observed mostly after the mechanical tests to investigate the effects of dislocations. After all mechanical tests, the cylindrical samples were cut in half lengthwise parallel to the axis, and the cross section was polished to a mirror finish by a microtome and observed using a confocal laser microscope (Optelics C130, Lasertec). Mean grain size was measured by the line intercept method with a correction factor of 1.5 (Underwood, 1970). Each specimen was analyzed in three positions, and the values attained were averaged (about 400 intercepts per sample). For samples #124 and #121A, microstructural observation was also performed before the mechanical tests, by polishing the top surface.

2.2. Experimental Apparatuses

Three different experimental apparatuses were used in this study: triaxial deformation apparatus, uniaxial forced oscillation apparatus, and ultrasonic testing apparatus. The triaxial deformation apparatus was used for the creep tests to determine the flow law and for deformation of samples before anelasticity tests (“creep”

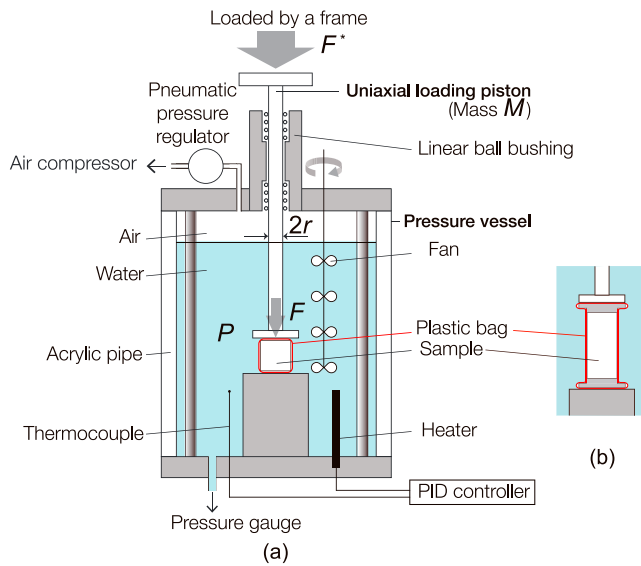


Figure 1. (a) Triaxial cell consisting of a pressure vessel and a uniaxial loading piston. The volume of air is compressed to provide up to 0.8 MPa of confining pressure in the vessel. This sample configuration was used for experiments described in sections 2.3 and 2.5. (b) Sample configuration for experiments described in section 2.4.

frame (sampling frequency was 1 Hz). We confirmed that friction on the piston was negligible by equivalent load values measured by inner and outer load cells. Differential load on the sample, F (N), was calculated as $F = F^* + Mg - F_p$, where F^* is the load applied by the loading frame, M ($=1.5$ kg) is the mass of the uniaxial loading piston, g is gravitational acceleration, and $F_p = \pi r^2 P$ is the upward force applied to the piston with radius r ($=10$ mm) by the confining pressure P in the pressure vessel (Figure 1). Based on the ability of the air compressor and the yield strength of the acrylic pressure cell, a maximum confining pressure of 0.8 MPa and differential stress $\Delta\sigma$ of 3 MPa can be applied to the samples.

The uniaxial forced oscillation apparatus used in this study is shown in Figure 2 and described fully elsewhere (Takei et al., 2014). Cyclic compressive loading tests from 10^2 to 10^{-4} Hz and creep tests can be performed under various temperatures ($0^\circ\text{C} \leq T \leq 50^\circ\text{C}$) and ambient pressure. The maximum differential stress $\Delta\sigma$ that can be applied to the samples by this apparatus is 0.28 MPa, which is much smaller than that needed for dislocation creep of borneol to be dominant.

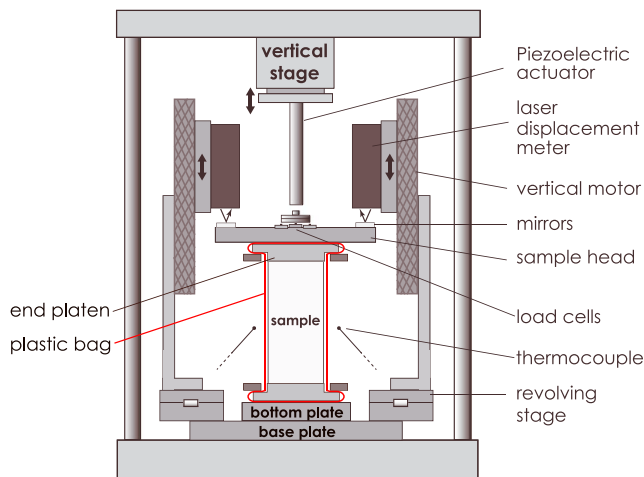


Figure 2. Forced oscillation apparatus. From Yamauchi and Takei (2016).

in Table 1). A confining pressure of 0.8 MPa was applied to suppress microcracking during dislocation creep of borneol samples. The forced oscillation apparatus was used for accurate measurement of anelastic properties under a small cyclic stress over a broad frequency range (10^2 – 10^{-4} Hz). The ultrasonic testing apparatus was used to nondestructively measure modulus and attenuation at 1 MHz.

In the triaxial deformation apparatus, a custom triaxial cell was placed in a commercial loading frame (Instron Co., Ltd., 5567, maximum load 3,000 kgf). Figure 1 shows a schematic illustration of the triaxial cell consisting of a pressure vessel (maximum confining pressure 1 MPa) and a uniaxial loading piston supported by a linear ball bushing (Tatsuoka, 1988). The pressure vessel is made of a thick transparent acrylic pipe that is reinforced with steel rods. The vessel was filled with water, leaving a small volume of air at the top. The pressure in the vessel was kept constant by connecting this air space to an air compressor through a pneumatic pressure regulator (Fairchild Co., Ltd., 10262U). The pressure in the vessel was monitored by a pressure gauge (Kyowa Co., Ltd., PGMC-A). Temperature inside the vessel (ambient $\leq T \leq 60^\circ\text{C}$) was monitored and controlled using a type K thermocouple and heater, which were connected to a proportional-integral-differential (PID) controller (Omron Co., Ltd., E5ER). The water in the vessel was stirred by circulating fans. Load F^* and displacement u of the loading piston of the vessel were measured by the load cell and encoder, respectively, of the loading

The ultrasonic testing apparatus is shown in Figure 2 in Takei (2000). Details of the apparatus used in this study are described in section 2.4 of Takei et al. (2014). In this study, this apparatus sits at room temperature and ambient pressure.

2.3. Flow Law Measurement

The steady-state deformation behavior of polycrystalline material is described by the semiempirical flow law relating strain rate $\dot{\epsilon}$ to stress $\Delta\sigma$, grain size d , and temperature T :

$$\dot{\epsilon} = A(\Delta\sigma)^n d^{-p} \times e^{-H/R_g T}, \quad (1)$$

where stress exponent n , grain size exponent p , and activation enthalpy H are specific to the deformation mechanism dominating at a given set of conditions. A and R_g represent a material constant and the gas constant, respectively. Since no previous deformation mechanism map has been developed for borneol, our first task was to explore the steady-state deformation behavior so as to determine the conditions at which dislocations are introduced into the sample by dislocation creep. Using the

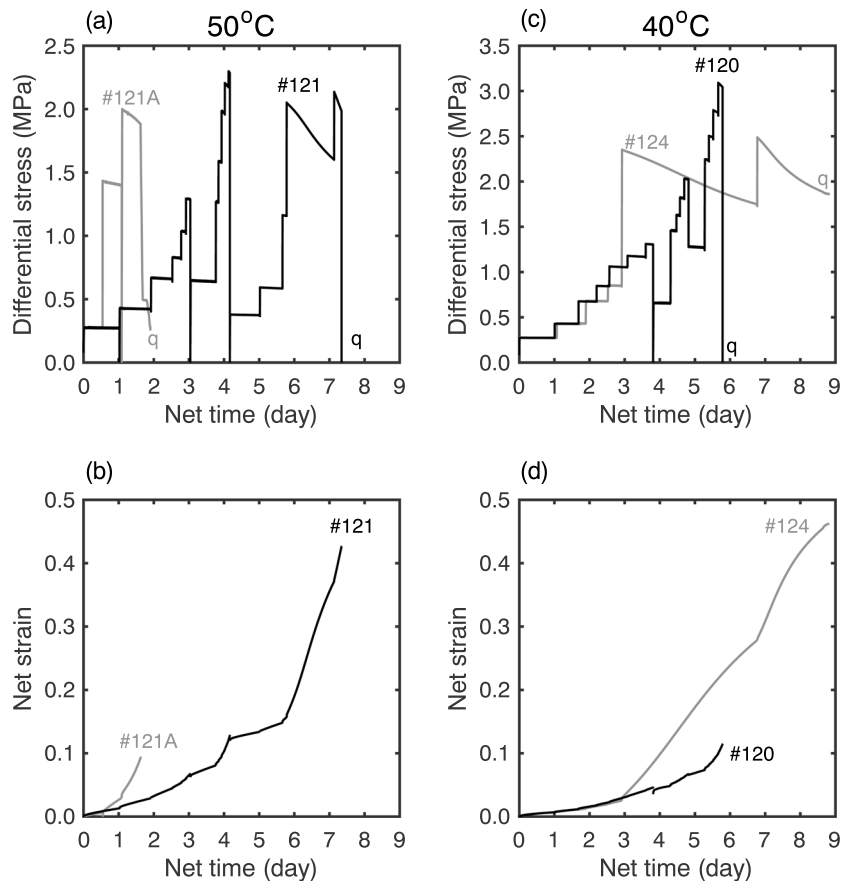


Figure 3. A series of creep tests performed on samples #120, #121, #121A, and #124: (a, c) differential stress and (b, d) net strain. Each creep test was performed under a constant differential load. Stepwise change in stress took about 10 min. Letter “q” in (a) and (c) means “quench.”

triaxial deformation apparatus, creep tests were performed under various differential stresses $\Delta\sigma$ from 0.28 to 3 MPa and a constant confining pressure of 0.8 MPa. Samples #120 and #124 were tested at 40 °C, and #121 was tested at 50 °C. An additional sample (#121A) was tested at 50 °C without confining pressure to check the sensitivity of the result to confining pressure.

Each sample was sealed in a nonreactive plastic bag and placed in the triaxial cell (Figure 1a). The plastic bag (thickness = 77 μm) prevents water invasion and also reduces the friction at the top and bottom surfaces of the sample. After filling the cell with water, temperature was increased to a run temperature. After a thermal equilibration (2 hr), confining pressure was increased to 0.8 MPa (with the exception of #121A) and kept constant. Then, mechanical tests were performed by changing the uniaxial load stepwise (within 10 min) to a relative maximum load, after which we removed the load. We refer to each stepwise segment as a creep test, such that a series of creep tests was performed on samples #120, #121, #121A, and #124 (Figure 3). For each k th creep test ($k = 1, 2, \dots$) performed under a constant differential load F (N), time-dependent sample length $L(t)$ was calculated from the initial length, L_i , and the displacement at t , $u(t)$, as $L(t) = L_i - u(t)$, where $t = 0$ represents the starting time of the first creep test. Strain rate $\dot{\epsilon}(t)$ was calculated as $\dot{u}(t)/L(t)$. Differential stress $\Delta\sigma(t)$ was calculated as $\Delta\sigma(t) = \frac{F}{\pi(R(t))^2}$, where sample radius $R(t)$ was calculated from the initial radius R_i and $L(t)$ by assuming a constant volume: $\pi R_i^2 L_i = \pi R^2(t) L(t)$. Under a constant F , $\Delta\sigma$ gradually decreases due to thickening of the sample (Figures 3a and 3c). The net strain shown in Figures 3b and 3d was calculated as $u(t)/L_i$.

After the last creep test on samples #120, #121, and #121A, we removed the axial load and confining pressure and quenched the sample to room temperature. We quenched samples #121 and #120 quickly by exposing them to cool tap water (#121) or room air (#120) and quenched #121A slowly by allowing the water in the cell to cool naturally using only the circulating fans inside the vessel (about 8 hr). In contrast, after the last

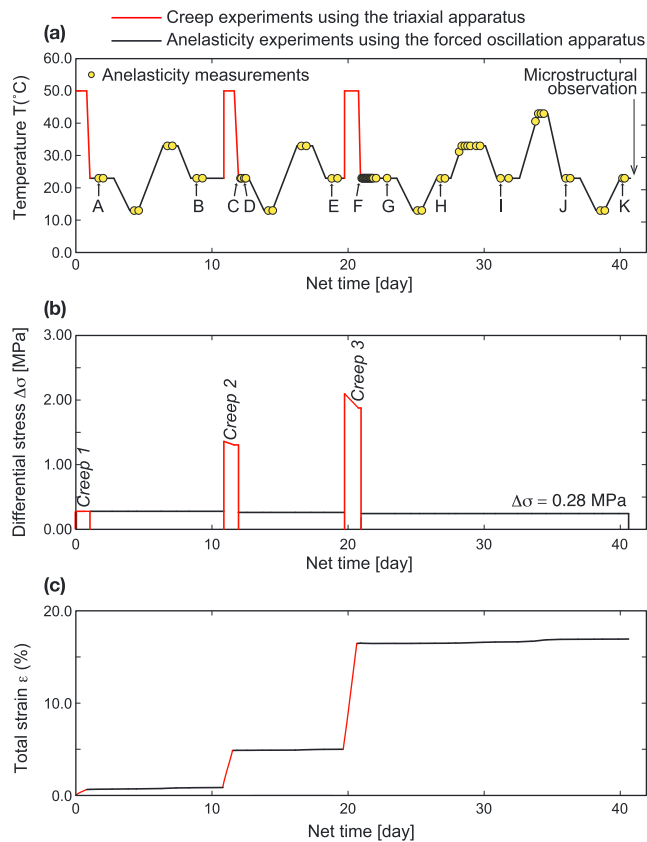


Figure 4. Temporal variation of (a) temperature, (b) differential stress, and (c) uniaxial strain of sample #122 during the experiment to investigate the effect of deformation (creeps 1–3) on anelastic properties. Creep 1–3 (red parts) were performed in the triaxial deformation apparatus (Figure 1b), and the other mechanical testing (black parts) were performed in the forced oscillation apparatus (Figure 2). Each yellow circle in (a) indicates an anelasticity measurement. The measurements marked by letters are referred to in section 3.2.1.

again. One yellow circle in Figure 4a represents a series of forced oscillation tests, in which Young's modulus E and attenuation Q^{-1} were measured for 8–20 frequencies between 68.1×10^{-4} Hz, where the highest eight frequencies between 68.1 and 1 Hz were always included. We repeated this measurement at each temperature, so that reproducibility of the data could be checked, and a temporal variation of anelasticity, if any, could be detected. The zero-to-peak amplitude of the cyclic stress and strain was less than 0.05 MPa and 2×10^{-5} , respectively. As shown in Figure 4b, in the forced oscillation apparatus, constant differential stress $\Delta\sigma = 0.28$ MPa was always applied to the sample. Therefore, we can also measure the diffusion creep viscosity of the sample (e.g., Takei et al., 2014). After all anelasticity measurements, we removed the sample unit from the forced oscillation apparatus and placed it again in the triaxial deformation apparatus to conduct the next increment of creep deformation (“creep 2” or “creep 3” in Figure 4b).

Creep 2 was conducted under $\Delta\sigma = 1.3$ MPa for 17 hr, and creep 3 was conducted under $\Delta\sigma \approx 2.0$ MPa for 23 hr, where the other conditions (temperature and confining pressure) were equal to those in creep 1. After each increment of creep, we quenched the sample and measured the anelastic property by following the same procedures as those after creep 1 but with a larger number of repetitions and for a wider temperature range (Figure 4a).

The data obtained by the forced oscillation tests were analyzed in the same manner as Takei et al. (2014). In the previous study, however, deformation of the sample was small ($\epsilon_{\text{fin}} \leq 0.016$), and hence in correcting the modulus data for the effect of no-slip boundary condition at the two end platens, the length/diameter ratio, $L/2R$, was fixed to 2.2. In this study, because $L/2R$ changes from 2.14 (after creep 1) to 1.67 (after

creep test on #124, the last (highest) axial load and confining pressure were maintained, while the water was allowed to slowly cool to room temperature using the circulating fans inside the vessel and an electric fan standing outside the vessel (about 6 hr). We then removed the axial load first and confining pressure next. This slow, and hence nondestructive, quench under the deviatoric stress was also used in the anelasticity experiments in sections 2.4 and 2.5. The final sample geometry (length and diameter at the top, middle, and bottom parts) was measured accurately to calculate final axial strain ϵ_{fin} and barrel distortion (Table 1).

2.4. Anelasticity Measurement of a Deformed Sample

In order to investigate the effect of dislocations on anelasticity, we performed forced oscillation experiments on a sample that was deformed in both the diffusion and dislocation creep regimes (as determined from the flow law study) and measured the resulting change in anelastic behavior. Figure 4 shows the variations of temperature, differential stress, and strain of sample #122 imposed during the testing protocol. The red parts in Figure 4 were conducted in the triaxial deformation apparatus (Figure 1), and the black parts were conducted in the uniaxial forced oscillation apparatus (Figure 2).

In order to conduct the multistep testing shown in Figure 4 on the single specimen, sample #122 (diameter = 30 mm, length = 65 mm) was assembled as follows. After attaching two brass end platens, the sample and platens were sealed in a nonreactive plastic bag, while air was removed by a vacuum pump. The end platens are needed to attach the sample tightly to the forced oscillation apparatus (Figure 2). The vacuum-sealed “sample + end platens” is hereafter referred to as the sample unit. We first placed the sample unit in the triaxial deformation apparatus (Figure 1b) and deformed the sample under differential stress $\Delta\sigma = 0.28$ MPa, confining pressure 0.8 MPa and temperature $T = 50^\circ\text{C}$ for about 19 hr (referred to as creep 1). Then, we quenched the sample under deviatoric stress (slow quench described in section 2.3, which takes about 6 hr), removed the sample unit from the triaxial cell, and attached it to the forced oscillation apparatus. As shown in Figure 4a, we then measured the anelastic property of this sample first at 20°C , then at 10 and 30°C , and finally at 20°C

creep 3), we derived the correction factor as functions of both Poisson's ratio and length/diameter ratio by conducting a numerical calculation (Appendix A). Also, the stiffness of the apparatus used in the data correction was measured by a blank test with a stainless steel sample that was superglued to the two end platens and vacuum sealed in a plastic bag.

Takei et al. (2014) estimated the random and systematic errors of Young's modulus measurements as <2% and less than or equal to ~3%, respectively. One of the important factors affecting this accuracy is contact between the sample and the two end platens. In this study, the sample unit was vacuum packed, so that perfect contact between the sample and the end platens, which is expected to be attained during creep 1, can be maintained even after removing the sample unit from the triaxial cell. In previous measurements of anelasticity with a plastic bag, air in the bag was not removed (McCarthy et al., 2011; McCarthy & Takei, 2011; Yamauchi & Takei, 2016), so that the plastic bag did not touch the sample. In that case, the bag did not affect the dissipation, as was confirmed by a comparison of the data to those obtained without a bag (e.g., Takei et al., 2014). In order to examine the effect of the vacuum-sealed bag on the anelasticity data, we cut the bag and let air in just before the first anelasticity measurement after creep 3 (just before run F in Figure 4a).

2.5. Ultrasonic Measurement of Samples Before and After Deformation

In order to constrain the characteristic frequency of the dislocation creep-induced anelasticity, we additionally measured the effects of deformation by dislocation creep on the elastic properties of samples #123 and #127 using ultrasonic testing. Each sample (diameter = 30 mm, length = 30 mm) was sealed in a nonre-active plastic bag; #123 was sealed by leaving some air in the bag, similarly to the samples in the flow law measurement in section 2.3, whereas #127 was sealed by removing air with a vacuum pump, similarly to #122 in section 2.4. In the same manner as the flow law measurement, each sample was placed in the triaxial cell (Figure 1a) and was deformed under $\Delta\sigma = 0.28$ MPa for 26 hr (creep 1), $\Delta\sigma \simeq 1.7$ MPa for 25 hr (creep 2), and $\Delta\sigma \simeq 2.0$ MPa for 16 hr (creep 3) in succession. Run temperature was 50 °C and confining pressure 0.8 MPa. We then quenched the sample under deviatoric stress (slow quench described in section 2.3) and removed it from the triaxial cell.

Before and after the deformation, longitudinal and shear wave velocities, V_p and V_s , of the sample were measured at room temperature (~ 22 °C) and ambient pressure by using the ultrasonic method. The velocities were calculated from P and S wave travel times and sample length. The sample length was measured directly (without a plastic bag) with a micrometer just before the ultrasonic test. Travel times were measured by the pulse transmission method by attaching transducers (PS-dual transducers D7054, Panametrics Inc., center frequency = 1 MHz) to the top and bottom surfaces of the sample, which was sealed in a plastic bag. The data were corrected for the time lags due to the transducers, plastic bag, and coupler, as described in Takei et al. (2014). From the measured V_p , V_s , and sample density (Table 1), Young's modulus at the ultrasonic frequency (1 MHz) was calculated. After ultrasonic testing was completed, we measured the final sample geometry and cut the sample for microstructural observation.

3. Results

First, in section 3.1, we summarize the mechanical and microstructural results of the creep tests performed on samples #120, #121, #121A, and #124 to determine the flow law of borneol. Then, in section 3.2, we summarize the results of forced oscillation and ultrasonic tests performed on the predeformed samples (#122, #123, and #127), where creep data during the prior deformation stage and microstructures of these samples are summarized in section 3.1.

3.1. Flow Law of Borneol

3.1.1. Creep Data

All creep curves obtained in the flow law measurement (Figure 3) are shown in Figures 5 and 6 by black and gray lines, where long creep curves obtained under high stress are shown in the latter. Several creep curves obtained during the creep tests performed before forced oscillation and ultrasonic tests are also shown in these figures by red (#122), blue (#123), and green (#127) lines to make up for the lack of long creep curves under medium stress around $\Delta\sigma \simeq 1.5$ MPa (Figure 5) and high stress around $\Delta\sigma \simeq 2$ MPa (Figure 6).

Most of the creep curves in Figure 5 show a transient creep and a steady-state creep, in which stress and strain rate were nearly constant (middle and bottom rows of Figure 5). These data can be used to determine the flow law and are plotted in Figure 7 as symbols. Figure 7 shows that the flow law at $\Delta\sigma < 1$ MPa follows

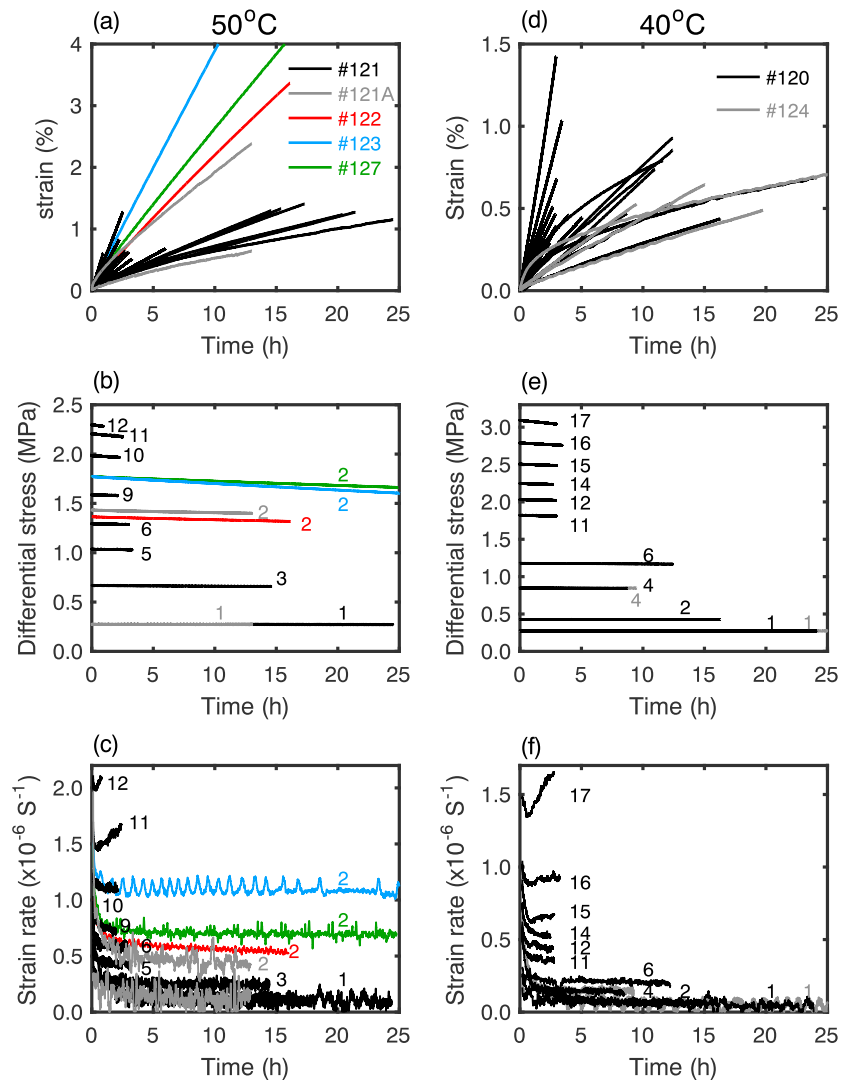


Figure 5. Results of the creep tests on #121 and #121A at 50 °C (left column) and on #120 and #124 at 40 °C (right column). (a,d) Strain, (b,e) differential stress (for selected creep tests), and (c,f) strain rate (for selected creep tests), versus time. Color shows sample, and number k near the curve shows the k th creep test on each sample (Figure 3). Some results from #122 (red), #123 (blue), and #127 (green) are also shown to make up for the lack of long creep curves under medium stress around $\Delta\sigma \simeq 1.5$ MPa. Sample #121A was deformed without confining pressure.

a linear stress-strain rate relationship (i.e., $n = 1$ in equation (1)), with viscosity $\eta = \Delta\sigma/\dot{\epsilon} = 2.8 \times 10^{12}$ Pas at 50 °C (#121) and 6.2×10^{12} Pas at 40 °C (#120 and #124). Consistency of this result with the previous result for high-purity borneol (Takei et al., 2014) is shown in Figure S2. Figure 7 also shows that the flow law at $\Delta\sigma > 1$ MPa deviates from a linear relationship. The emergence of a nonlinear flow law (i.e., $n > 1$ in equation (1)) at higher stress can be also confirmed by wider vertical spacing in the strain rate plots (Figures 5c and 5f) than that in the stress plots (Figures 5b and 5e).

The three creep curves in Figure 5 obtained under the highest two stresses at 50 °C (creeps 11 and 12 on sample #121) and the highest stress at 40 °C (creep 17 on #120) showed a different behavior from the others: The initial strain-hardening stage was followed by a strain-weakening stage (Figures 5c and 5f), and steady-state creep was not observed. For these three tests, the stress-strain rate data at the end of the initial strain-hardening stage (i.e., at the point of minimum strain rate) were plotted in Figure 7 by circular symbols with an attached bar, such that the free end point of the bar indicates the data at the end of each creep test. Although these bars are short, if these creep tests had been performed for a longer time interval, the bars would have been longer. For a detailed investigation of the strain weakening stage, we performed four

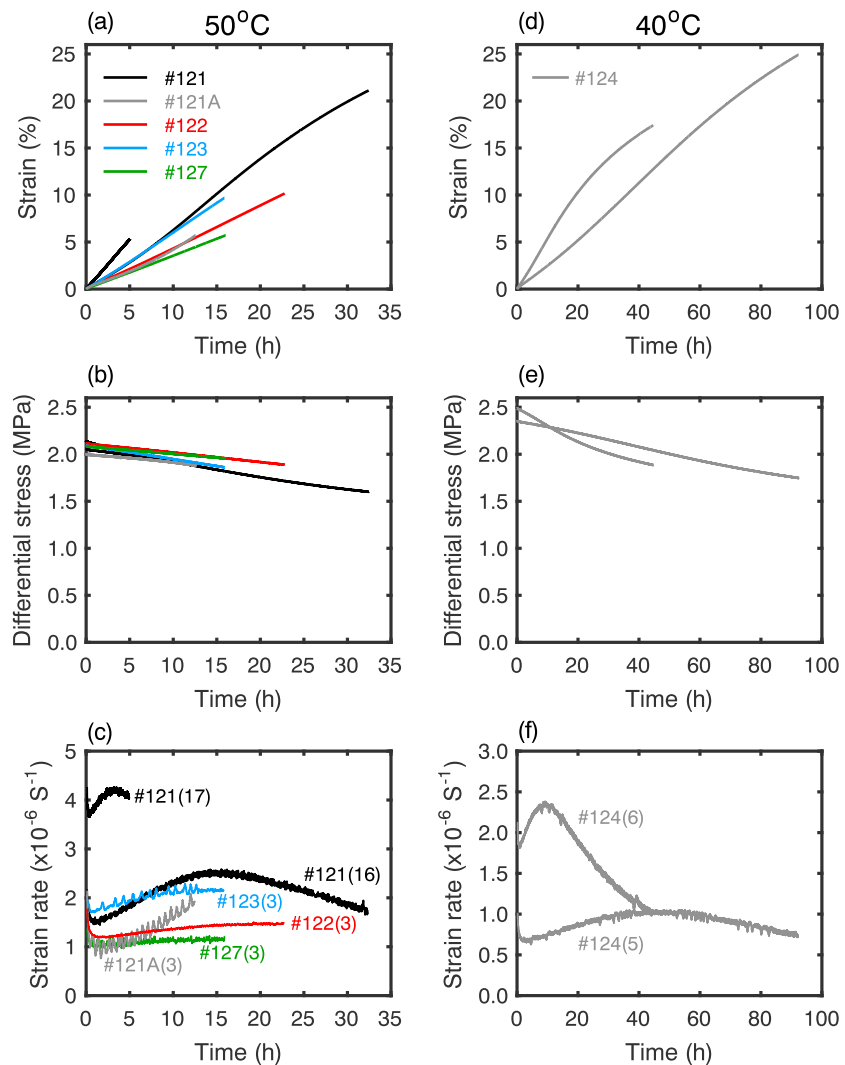


Figure 6. Results of the creep tests performed for a long time under high stress ($\Delta\sigma \approx 2$ MPa). (a,d) Strain, (b,e) differential stress, and (c,f) strain rate, versus time. Color shows sample, and number k in the parentheses in (c) and (f) shows the k th creep test on each sample. Sample #121A was deformed without confining pressure.

very long creep tests under high stress (creeps 16 and 17 on #121 and creeps 5 and 6 on #124). As typically shown by creep 16 of #121 (Figure 6c) and creep 5 of #124 (Figure 6f), the obtained creep curves consisted of three stages: initial deceleration stage, second acceleration stage, and final deceleration stage. Because steady-state creep was not obtained at these high stresses, in order to estimate the steady-state flow law, it is important to clarify the physical processes responsible for the three stages.

When a creep test is conducted under a constant load, stress gradually decreases due to thickening of the sample. When stress is high, this thickening and hence the stress reduction are fast (Figures 6b and 6e). Because strain rate is sensitive to stress at high stress, the final deceleration stage can be explained well by the response of the sample to the stress reduction. In other words, the third deceleration stage is not considered to represent an intrinsic property of the sample. In contrast, it is not evident whether the second acceleration stage represents an intrinsic or extrinsic process of the sample. Strain weakening prior to steady-state dislocation creep was reported in the deformation experiments of olivine single crystals (Cooper et al., 2016; Hanson & Spetzler, 1994), indicating the time-dependent evolution of dislocation density or dislocation microstructure in the deforming crystals. A similar process, if active in borneol crystal, can explain the strain weakening stage, while the first strain-hardening stage preceding it may be explained by a similar mechanism to the transient creep in the diffusion creep regime (i.e., diffusively accommodated grain

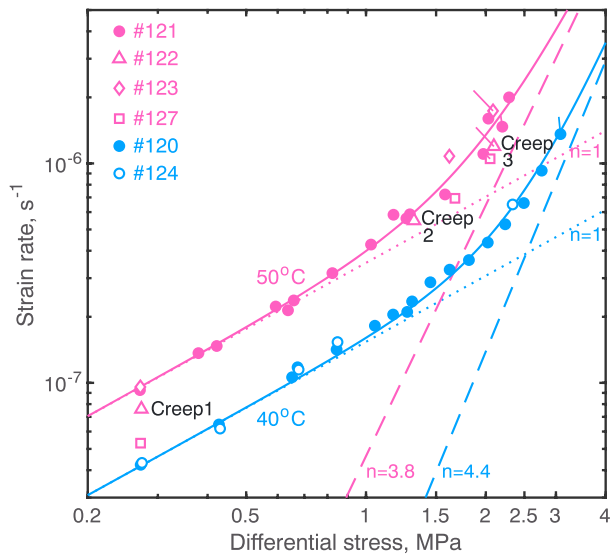


Figure 7. Flow law of polycrystalline borneol. Color shows temperature (pink = 50 °C, blue = 40 °C), and symbol type corresponds to a sample. The pink and blue solid curves show the best fit models obtained from the data of #121 (50 °C, pink) and #120 (40 °C, blue), which are composed of linear creep (dotted line) and power law creep (dashed line). Symbols with a bar indicate tests at high stress where samples demonstrated a strain weakening stage, such that the stress and strain rate conditions just before the strain weakening stage are shown by the symbol and the conditions at the end of the creep tests are shown by the free end point of the bar.

tude of strain weakening showed a good correlation with the effective confining pressure (Figures 6c and 6f), suggesting the extrinsic origin (due to microcracks or pores) of the strain weakening stage. This result was also supported by the microstructural observation in section 3.1.2. Therefore, we do not use the data obtained during and after the weakening stage in determining the steady-state flow law in Figure 7.

The intrinsic creep strength around $\Delta\sigma \approx 2$ MPa may be best estimated by the stress and strain rate data just before the weakening stage. For creep 16 on #121 and creep 5 on #124, such data were plotted in Figure 7 by circular symbols, whereas creep 17 on #121 and creep 6 on #124 after experiencing a significant strain weakening (more than 20% strain) were not used in the flow law analyses. The data from #121A were not used, because #121A had larger grain size than the others (Table 1). We estimated the steady-state flow law at 50 and 40 °C by fitting the formula

$$\dot{\epsilon} = \Delta\sigma/\eta + B\Delta\sigma^n \quad (2)$$

to the data sets obtained from #121 and #120, respectively, where the values of η estimated in the linear range were used. The best fit results are presented in Table 2 and plotted in Figure 7 (pink and blue lines).

3.1.2. Microstructure of the Deformed Samples

We first report the results of microstructural observation supporting the occurrence of dislocation creep indicated by the emergence of power law creep. We then report the observation of microcracks and/or pores indicated by the emergence of the strain weakening stage.

Figures 8a and 8b show the microstructure of sample #124 before and after deformation. During the high-temperature annealing (for grain growth) performed before the deformation, microstructure was equilibrated to minimize interfacial energy. As shown in Figure 8a, grain boundaries in the undeformed sample

Table 2

Flow Law Parameters in Equation (2)

	η	n	B
50 °C (#121)	2.8×10^{12} Pas	3.8	$4.226 \times 10^{-8} (\text{MPa})^{-3.8} \text{ s}^{-1}$
40 °C (#120)	6.2×10^{12} Pas	4.4	$6.587 \times 10^{-9} (\text{MPa})^{-4.4} \text{ s}^{-1}$

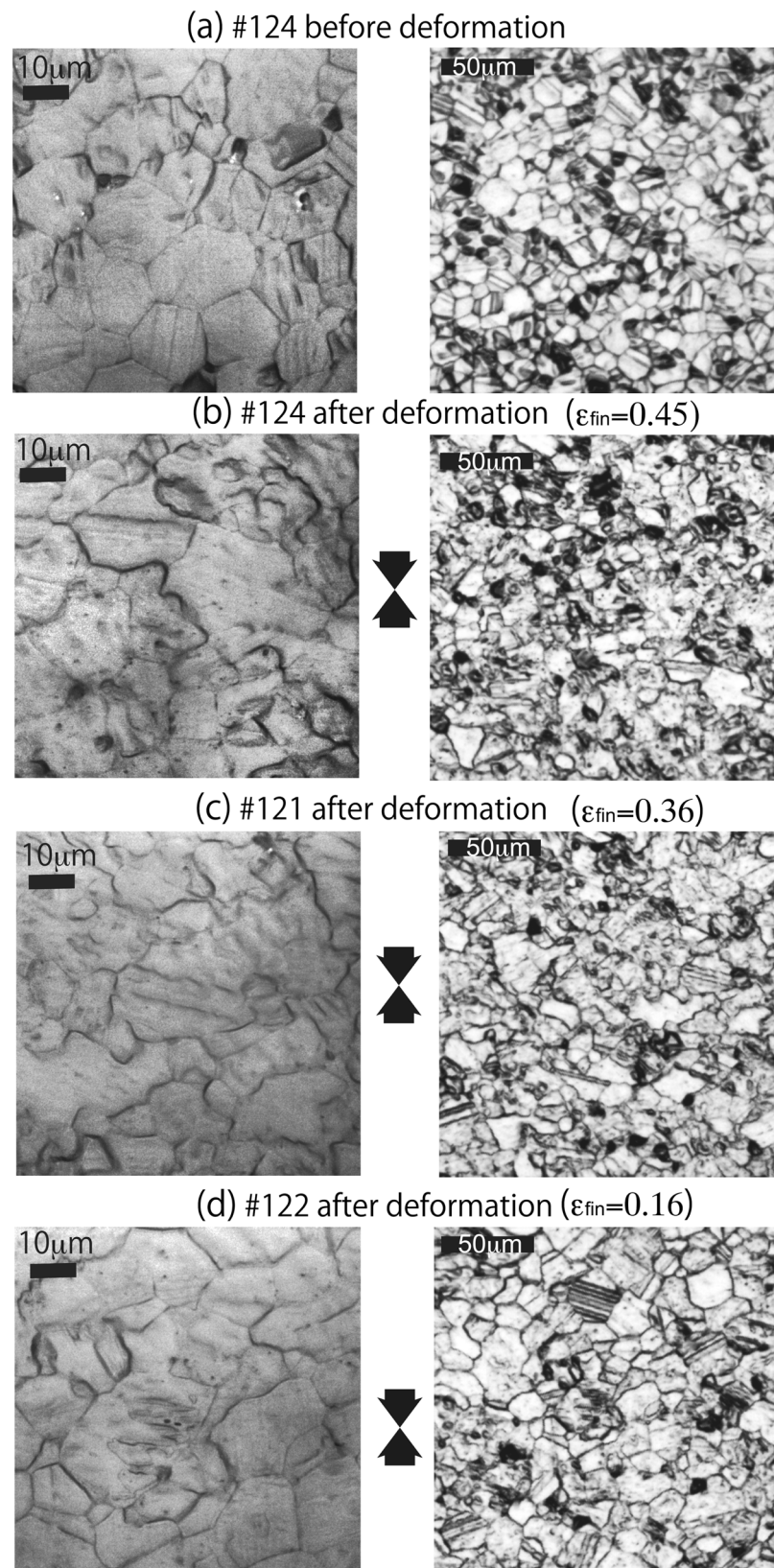


Figure 8. Light microscopic images of polycrystalline borneol at high and low magnification. (a,b) Sample #124 before and after deformation. (c,d) Samples #121 and #122 after deformation. (b)–(d) show the images near the center part of the samples. Arrows show the uniaxial compression direction.

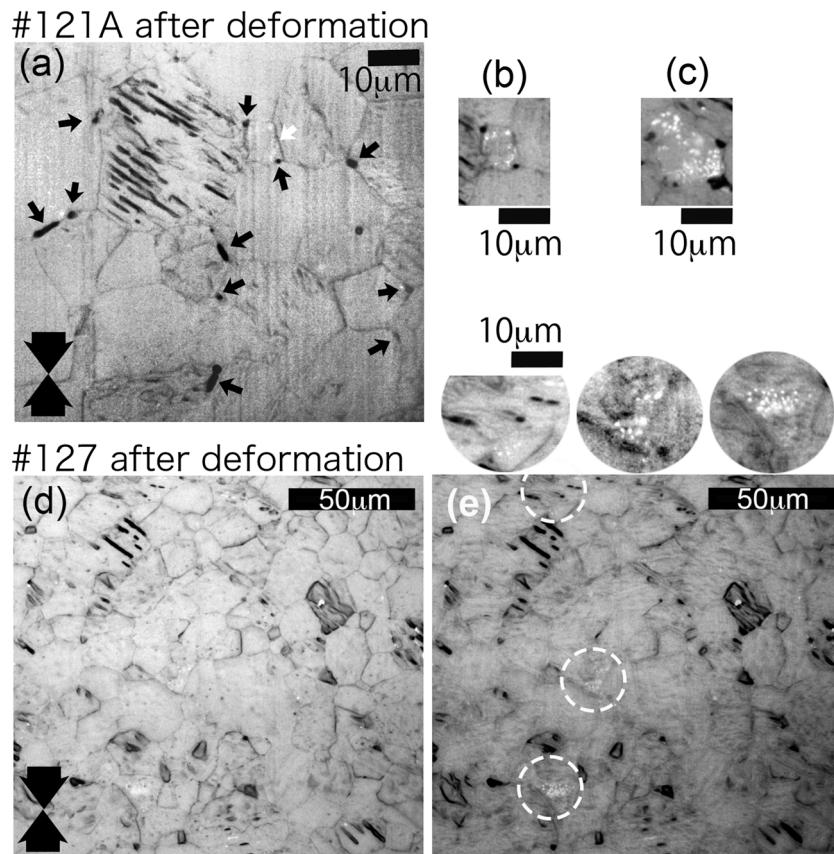


Figure 9. Light microscope images of samples #121A and #127 observed near the outer cylindrical surface. (a–c) Microstructures of #121A deformed without confining pressure. (d, e) Microstructures of #127 deformed with confining pressure. Thick black arrows in (a) and (d) show the uniaxial compression direction. Small black arrows in (a) show deformation-induced micropores, and white arrow shows the grain in (b). The faint spots in (b) and (c) can be interpreted as pores in the near subsurface. (e) was obtained by focusing the microscope to a depth 1 μm below the surface shown in (d). Faint spots similar to (c) are found in the dashed circles, for which enlarged and highly contrasted views are provided above (e).

are observed mostly as straight lines, which intersect at about 120° at the triple junctions. Grains are mostly polygonal and equi-axial. In contrast, after the creep tests in the power law regime, the boundaries are observed as wavy lines, and the angles at the triple junctions frequently deviate from 120° (Figure 8b). Irregularly shaped grains, sometimes elongated in the horizontal direction, were observed frequently. The microstructure observed after diffusion creep was similar to the equilibrium microstructure in Figure 8a (Figure 4b–d in Takei et al., 2014). Hence, the disequilibrium microstructure in Figure 8b indicates the occurrence of dislocation-induced grain boundary migration. We did not observe a remarkable change in grain size by dislocation creep.

The deviation from the equilibrium microstructure tends to increase with increasing final strain and/or temperature. As shown in Figure 8c, similar disequilibrium texture in #124 ($\epsilon_{\text{fin}} = 0.45$, 40°C) was observed in #121 ($\epsilon_{\text{fin}} = 0.36$, 50°C) both of which were deformed to similarly high strains. Whereas in the microstructure of #121A ($\epsilon_{\text{fin}} = 0.09$), #122 ($\epsilon_{\text{fin}} = 0.16$), #123 ($\epsilon_{\text{fin}} = 0.21$), and #127 ($\epsilon_{\text{fin}} = 0.13$) deformed at 50°C , the deviation from the equilibrium texture was small compared to #121 and #124. A typical microstructure of these low strain samples is shown in Figure 8d, and from these samples, we obtained grain size measurements. However, the linear intercept method does not work well with wavy grain boundaries, since each grain can cut a line more than twice. Hence, we measured grain size only for the near-equilibrium microstructures (Table 1).

Figures 9a–9c show microstructures of sample #121A deformed without confining pressure. These figures were obtained near the outer cylindrical surface. We observed micropores (pores much smaller than grain size) at or near triple junctions and along grain boundaries (marked by small black arrows). The grain in

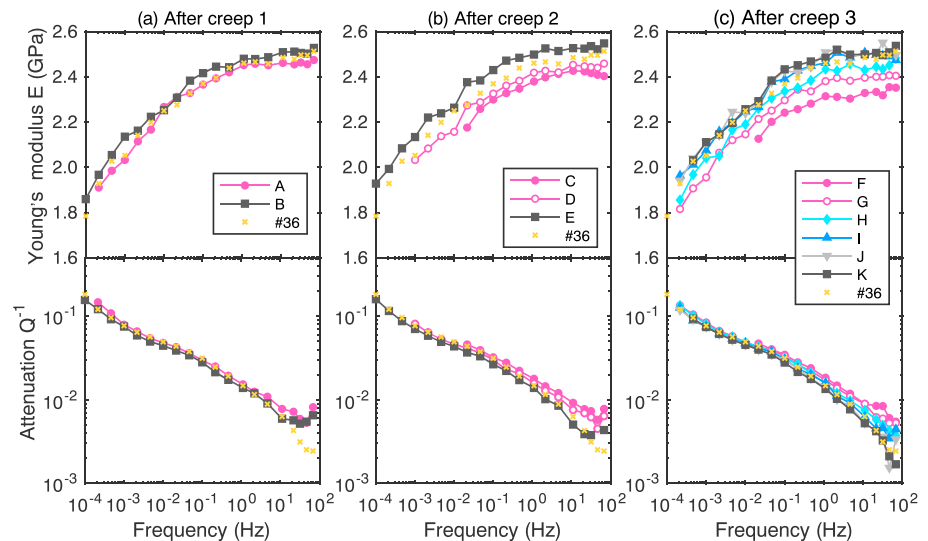


Figure 10. Young's modulus and attenuation versus frequency of sample #122 measured after (a) creep 1 in the diffusion creep regime, (b) creep 2 with some contribution from dislocation creep, and (c) creep 3 with the largest contribution from dislocation creep (pink open triangles in Figure 7). All data shown in these figures were obtained at 20 °C. Alphabetic data set labels indicate the timing of the measurement described in Figure 4a. Pink circular and black square symbols show the data in the first and the last 20 °C testing, respectively, after each creep. Yellow cross symbols show the previous data by Takei et al. (2014; sample #36, $d = 15.9 \mu\text{m}$).

Figure 9a labeled by the white arrow is shown in Figure 9b, where the faint spots can be interpreted as pores in the near subsurface. We occasionally observed multiple micropores on a single grain boundary (Figure 9c), which may be called a crack. Based on these observations, we consider that the physical process responsible for the strain weakening stage was formation of micropores and cracks, which also explains well the observed sensitivity to the effective confining pressure. Because the strain weakening stage was slower at lower temperature (Figures 6c and 6f), it may be a more ductile process than brittle fracturing. Micropores and cracks were mostly found within 1 mm of the outer cylindrical surface, were only occasionally found inside the cylinder, and rarely found near the top and bottom surfaces. Consistently, transparency of sample #121A was not lost even after the deformation (Figure S1).

Figures 9d and 9e show the microstructures of sample #127 deformed under the effective confining pressure of 0.8 MPa. The strain weakening stage was much smaller in amplitude than #121A, which had no confining pressure (Figure 6c). Indeed, micropores similar to Figure 9a were rarely recognized in this sample. Nevertheless, we did observe some cracks. Figure 9e was obtained by focusing the microscope on the subsurface plane at a depth of 1 μm beneath that shown in Figure 9d. We could find multiple micropores indicating cracks (dashed circles in Figure 9e). Figures 9d and 9e were obtained near the outer cylindrical surface. Inside the cylinder, we found only one or two of such cracks per $S = 284 \times 227 (\mu\text{m})^2$. By assuming that these cracks are 45° to the compression axis (i.e., shear cracks), and mean radius a is given by $a = d/2 \approx 10 \mu\text{m}$, the number density N is estimated as $N = (1 \sim 2)/(Sd/\sqrt{2}) (\mu\text{m})^{-3}$. Then, crack density parameter $c = Na^3$ (e.g., O'Connell & Budiansky, 1974) can be semiquantitatively estimated as $c = 0.002\text{--}0.004$. Even under the highest effective confining pressure, deformation in the dislocation creep regime is not free from microcracking. In #121A, micropores were more remarkable than microcracks, probably because #121A was slowly quenched without deviatoric stress, and hence, thin cracks were able to heal.

3.2. Effects of Dislocation Creep on Anelasticity

3.2.1. Results of Forced Oscillation Tests

The stress and strain rate conditions of the deformation of sample #122 prior to the forced oscillation tests are shown in Figure 7 (pink open triangles labeled creeps 1–3). Creep 1 is in the diffusion creep regime, creep 2 is transitioning into dislocation creep, and creep 3 is also transitioning but has the largest contribution from dislocation creep. Young's modulus E and attenuation Q^{-1} measured after creeps 1–3 are shown in Figures 10a–10c, respectively, where only the data at 20 °C are plotted. Pink circular symbols show the data of the first 20 °C testing after each creep (solid pink and open pink circles in Figures 10b and 10c show,

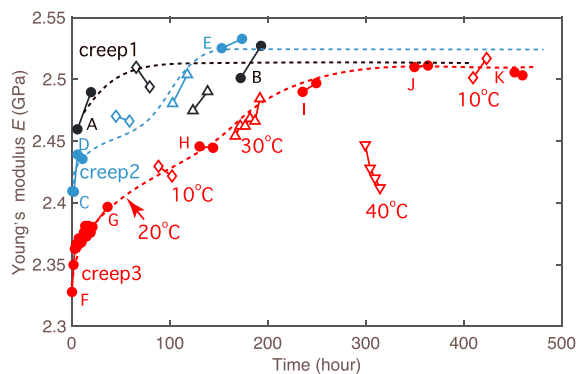


Figure 11. Recovery of Young's modulus during the repeated anelasticity measurements after creep 1 (black), creep 2 (blue), and creep 3 (red) performed on sample #122 is shown as time series data. Each symbol shows the average of the modulus over the same eight frequencies from 68.1 to 1 Hz. Solid circles show the data at 20 °C, open diamonds 10 °C, open triangles 30 °C, and open reverse triangles 40 °C. Letters are equal to those in Figure 4a. Dashed lines are schematic recovery curves showing E at 20 °C versus time (see text for detail).

respectively, the first and last data of the repeated measurements), and black square symbols show the data of the final 20 °C testing. Also shown in Figure 10c are the data of the second (light blue diamond), third (blue triangle), and fourth (gray reverse triangle) 20 °C testings showing an evolution with time. Figure 10 clearly shows that the Young's modulus E was significantly reduced and attenuation Q^{-1} was slightly increased after deformation by dislocation creep and that the magnitude of these changes systematically depends on the deviatoric stress amplitude of the prior deformation. Moreover, modulus E gradually increased and attenuation Q^{-1} gradually decreased during the repeated anelasticity measurements and finally recovered to the values obtained after creep 1, that is, the values before dislocation creep. These final data (black square symbols in Figures 10a–10c) agree well with the previous data of a high-purity borneol sample with similar grain size (yellow cross symbols in Figure 10).

Figure 11 plots the time series data showing the recovery of Young's modulus E . All data points in this figure show the average E over the highest eight frequencies (from 68.1 to 1 Hz), so that the effect of data scattering is removed. In addition to the data at 20 °C (solid circle), those at 10 °C (open diamond), 30 °C (open triangle), and 40 °C (open reverse triangle)

are shown. Because modulus data tend to decrease with increasing temperature (mostly due to the anelastic effect; e.g., McCarthy et al., 2011; Takei et al., 2014), by using the 10 °C symbols as an upper bound and 30–40 °C symbols as a lower bound, we estimated the recovery curves connecting the modulus at 20 °C (dashed lines). The recovery curves after creeps 2 and 3 clearly show that the recovery slows down at lower temperature (10 °C) and is enhanced at higher temperature (30 °C).

The present results show that the deformation under high differential stress ($\Delta\sigma > 1$ MPa) reduced the Young's modulus and slightly increased the attenuation, but these effects mostly disappeared over the course of the anelasticity measurements performed under the small differential stress ($\Delta\sigma = 0.28$ MPa). Although Young's modulus generally depends on both bulk and shear moduli, because of the large Poisson's ratio of borneol ($\nu = 0.371$, Takei, 2000), it is quite insensitive to the bulk modulus (McCarthy et al., 2011). Therefore, the observed change in the Young's modulus can be attributed to the change in the shear modulus.

The previous data (yellow cross symbols in Figure 10) follow the Maxwell frequency scaling and hence can be associated with diffusionally accommodated grain boundary sliding (McCarthy et al., 2011; Takei et al., 2014). The deviation from this grain boundary-induced anelasticity in the predeformed samples gives the dislocation creep-induced anelasticity, which appeared largely in the modulus and only slightly in the attenuation spectra. Due to the relationship between modulus dispersion and attenuation (e.g., equations 11 and 12 in Takei et al., 2014), this result indicates that the characteristic frequency of the dislocation creep-induced anelasticity is higher than 68.1 Hz (the highest frequency of the forced oscillation data) and hence much higher than the major part of the dissipation band caused by the grain boundary sliding. Further constraint on the characteristic frequency is given by the ultrasonic data. As shown in Figure 8d, sample #122 after all mechanical tests had wavy grain boundaries. Because the anelasticity data obtained after the recovery agreed well with those after creep 1 and also those in the previous studies, we can say that the small deviation from the equilibrium microstructure (wavy grain boundaries) does not significantly affect grain boundary sliding.

In Figures 10a and 10b, we observe a slight increase in attenuation Q^{-1} with increasing frequency above 10 Hz, which is not observed in the Q^{-1} data in Figure 10c measured after releasing the vacuum of the plastic bag. Because the Q^{-1} spectra in Figure 10c agree well with the previous data without a plastic bag (yellow cross symbols), the slight increase in Q^{-1} above 10 Hz can be considered an effect of the vacuum-sealed plastic bag.

In the forced oscillation apparatus, diffusion creep viscosity was measured just before each change in the run temperature (Figure 4a). (Viscosity was not measured at 10 °C.) The effect of prior deformation by dislocation creep on the diffusion creep viscosity was not visible, and the obtained viscosity data were consistent with the previous result without dislocations (Figure S2). This is consistent with the above mentioned

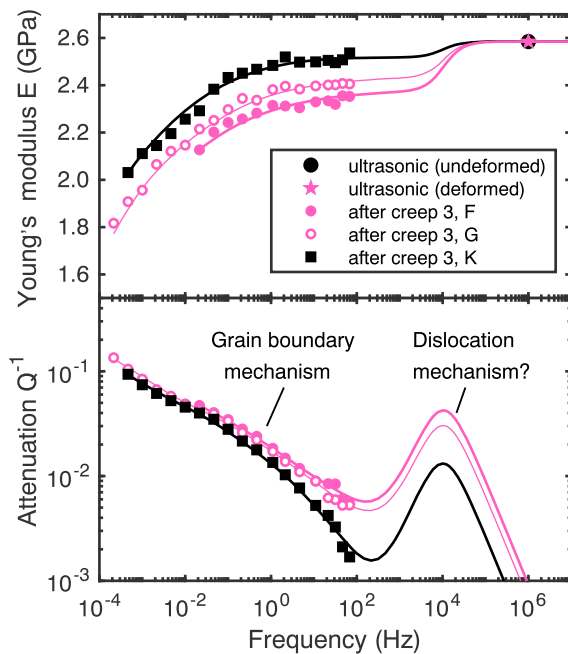


Figure 12. A possible distribution of the dislocation creep-induced anelasticity obtained from a combined analysis of both ultrasonic and forced oscillation data. Major part of the dislocation creep-induced dissipation is a peak at much higher frequency than the high-temperature background that is dominant at $f \leq 100$ Hz, which is attributable to grain boundary sliding. Symbols show the experimental data ($T = 20^\circ\text{C}$, homologous temperature $T/T_m = 0.61$, and Maxwell frequency $f_M \approx 1.3 \times 10^{-5}$ Hz). Each set of solid curves (E and Q^{-1}) was calculated from an appropriate relaxation spectrum.

equation (9) in Takei et al. (2014). Unrelaxed modulus was given by the ultrasonic result ($E_U = 2.585$ GPa), which agrees well with a previous value ($E = 2.600$ GPa, Takei et al., 2014). In this study, unlike Takei et al. (2014), a line spectrum was added to $X(\tau)$ at $\tau = (2\pi \times 10^4)^{-1}$ s, in order to make up the modulus deficit between $f = 10^6$ and $f \leq 68.1$ Hz. Therefore, the calculated Q^{-1} spectrum includes a Debye peak with the center frequency at $f = 10^4$ Hz. The assumption of a line spectrum was used for mathematical simplicity and is modified below. Figure 12 demonstrates that major part of the dislocation creep-induced anelastic relaxation forms a peak at much higher frequency than the major part of high-temperature background, which is caused by diffusionally accommodated grain boundary sliding.

Figure 12 also shows that the Debye peak is gradually reduced by annealing, but some part of it ($\sim 30\%$) remains even after the recovery (black peak). This result might mean that once deformed in dislocation creep, the borneol samples always contain some dislocations that cannot be removed by high-temperature annealing. However, because a small modulus deficit similar to that of data “K” ($\sim 3\%$), which is covered by the black peak in Figure 12, exists even without dislocation creep (Figure 17a in Takei et al., 2014), it might be alternatively explained by elastically accommodated grain boundary sliding and/or a systematic error of the modulus measured by the forced oscillation test (Takei et al., 2014).

The Debye peak in Figure 12 resulted from the line spectrum assumption of $X(\tau)$ introduced for mathematical simplicity. However, as shown in Figure S4, even if a broader distribution of relaxation time is assumed, the anelasticity induced by dislocation creep is a peak at much higher frequency than the major part of the high-temperature background. Therefore, the major conclusion of this section does not depend on the assumed form of $X(\tau)$.

4. Discussion

4.1. Dislocation Creep

The newly obtained creep data show that the dominant deformation mechanism of high-purity borneol starts to transition from diffusion to dislocation creep at $\Delta\sigma \approx 1$ MPa for $T = 40\text{--}50^\circ\text{C}$. At high stress

observation that the effect of deformation by dislocation creep on the low frequency attenuation is very small.

3.2.2. Result of the Ultrasonic Test

The stress and strain rate conditions during the deformation of samples #123 and #127 were plotted in Figure 7 (pink open diamonds and squares). The conditions of the last, highest stress creep on these samples were similar to that in creep 3 of #122, and hence, dislocation-creep effects similar to those on #122 by creep 3 can be expected. Typical ultrasonic wave forms obtained before and after the deformation are shown in Figure S3. For sample #123 (which was deformed to $\epsilon_{\text{fin}} = 0.21$ at $\Delta\sigma \leq 2.1$ MPa), we obtained $V_p = 2.222$ km/s, and $V_s = 0.963$ km/s, and hence, $E = 2.585$ GPa before the deformation, and $V_p = 2.223$ km/s, and $V_s = 0.963$ km/s, and hence, $E = 2.585$ GPa after the deformation. For #127 (which was deformed to $\epsilon_{\text{fin}} = 0.13$ at $\Delta\sigma \leq 2.1$ MPa), we obtained $V_p = 2.217$ km/s, $V_s = 0.965$ km/s, and $E = 2.596$ GPa before the deformation, and $V_p = 2.214$ km/s, $V_s = 0.963$ km/s, and $E = 2.588$ GPa after the deformation. By considering the errors of $\pm 0.15\%$ in V_p and $\pm 0.2\%$ in V_s (Takei et al., 2014), for both samples, Young's modulus measured at ultrasonic frequency (1 MHz) did not show any significant change after dislocation creep. The waveforms did not show any visible increase in attenuation at ~ 1 MHz (Figure S3). These results show that the major part of the dislocation creep-induced anelastic relaxation exists at frequencies lower than 1 MHz.

A possible distribution of the dislocation creep-induced anelasticity, explaining both ultrasonic and forced oscillation data, is shown in Figure 12 (solid curves). Each set of curves (E and Q^{-1}) was calculated from a relaxation spectrum $X(\tau)$ (Nowick & Berry, 1972) estimated as follows. First, from the modulus and attenuation data obtained by the forced oscillation test, we estimated the relaxation spectrum $X(\tau)$ by using

around $\Delta\sigma \simeq 2$ MPa, the initial hardening stage was followed by a strain weakening stage. Based on the sensitivity to the effective confining pressure and also based on the results of microstructural observations, we attributed the strain weakening stage to a growth of microcracks and/or pores, particularly near the outer cylindrical surface of the sample. Therefore, the data during and after the strain weakening stage were not used in determining the steady-state flow law provided in Figure 7 and Table 2. The stress exponent of steady-state dislocation creep was estimated as $n \simeq 4$. The microstructure of the deformed samples showed wavy grain boundaries, indicating the occurrence of dislocation-induced grain boundary migration. Here we compare the present results with transient and steady-state creep of olivine in the dislocation creep regime, experimentally studied in single crystals (Cooper et al., 2016; Hanson & Spetzler, 1994) and polycrystals (Chopra, 1997; Hansen et al., 2012).

Similar to the present result, grain boundary migration indicated by serrated grain boundaries is generally reported for olivine polycrystal (e.g., Mei & Kohlstedt, 2000). The observation of inverse transients, or strain weakening, in the dislocation creep of olivine is limited but to a few cases: deformation of single crystals with constant axial load in the direction of $[110]_c$ (Hanson & Spetzler, 1994) and with constant axial stress in the direction of $[011]_c$ (Cooper et al., 2016). Even in these cases, however, strain weakening did not exceed a few percent strain. Olivine polycrystals generally show strain hardening (Chopra, 1997). Only at large strain do olivine polycrystals show strain weakening mostly due to a grain-size evolution by recrystallization (Hansen et al., 2012). However, grain-size evolution was not observed in the present study. Therefore, with the present conclusion that the strain weakening process observed in our study was not intrinsic (i.e., was due to microcrack and/or pore formation), we can remove the extrinsic weakening, and the resulting transient behavior of polycrystalline borneol is similar to that of polycrystalline olivine. Furthermore, the stress exponent measured during steady-state dislocation creep of olivine single crystals and polycrystals is obtained as 3–4 (e.g., Cooper et al., 2016; Hansen et al., 2012; Mei & Kohlstedt, 2000), which is also similar to that of polycrystalline borneol obtained in this study.

4.2. Dislocation Creep-Induced Anelasticity

As shown in Figure 12, following deformation by dislocation creep, a large peak in the attenuation spectra is presumed to exist at high frequency, which gradually decreased during the anelasticity measurements under low differential stress ($\Delta\sigma \simeq 0.28$ MPa). We first compare the present anelasticity results with that obtained for the same material (borneol polycrystals) in which the grain-boundary mechanism was isolated. Anelastic relaxation by grain boundary sliding at various temperatures, grain sizes, and chemical compositions can be characterized by two nondimensional parameters; normalized frequency f/f_M and homologous temperature T/T_m , where $f_M = E_U/\eta$ represents the Maxwell frequency calculated by unrelaxed Young's modulus E_U and diffusion creep viscosity η and T_m represents the melting temperature or solidus (Takei, 2017). The data in Figure 12 (sample #122 at $T = 20^\circ\text{C}$) have $T/T_m = 0.61$ and $f_M \simeq 1.3 \times 10^{-5}$ Hz, where we used $\eta = 2.0 \times 10^{14}$ Pas measured in the forced oscillation apparatus at 20°C (Figure S2). Therefore, using this same Maxwell frequency normalization on the data in Figure 12, the peak at $f = 10^4$ Hz is $f/f_M \simeq 10^9$. A large and broad high-frequency peak caused by a grain boundary mechanism has been previously captured in borneol (+diphenylamine) at near solidus temperatures $T/T_m > 0.9$, which was attributed to grain boundary premelting (Takei, 2017; Yamauchi & Takei, 2016). However, when $T/T_m = 0.61$, grain boundary effects mostly exist at $f/f_M < 10^5$ as high-temperature background (e.g., Figure 9d in Takei et al., 2014), which corresponds to $f < 1$ Hz in Figure 12. Therefore, dislocation creep-induced anelasticity obtained in this study has a much shorter relaxation time scale than that of grain boundary effects at this low homologous temperature.

As shown in section 3.1.2, dislocation creep in this study was not completely free from microcracking. For mantle rocks, the empirical condition for fully plastic deformation without any contribution from microcracks is known as $\sigma_3 \geq \sigma_1 - \sigma_3$, where σ_1 and σ_3 represent, respectively, the largest and smallest compressive principal stress (e.g., Evans et al., 2016). This condition, called the Goetze criterion, was not satisfied in this study ($\sigma_1 - \sigma_3 \simeq 2$ MPa and $\sigma_3 = 0.8$ MPa). Higher confining pressure is needed to completely suppress microcracking. Although the emergence of the nonlinear creep and the wavy grain boundaries indicate the presence of dislocations, the obtained change in the anelastic properties cannot be solely attributed to the dislocations. If we estimate the effect of microcracks on Young's modulus by using the observed crack density parameter ($c = 0.002$ – 0.004) and poroelastic theory (O'Connell & Budiansky, 1974), the modulus reduction is estimated as 0.15–0.3% for closed cracks and 0.33–0.66% for open cracks. (Calculations are given in Supporting Information S1). Although the estimated reduction by microcracks is much smaller than the

observed modulus change, this estimation based on the visible microcracks can be an underestimation. We cannot deny a possible existence of grain boundary cracks which were completely closed and invisible after the removal of stress but still affect the grain boundary sliding. The observed recovery of the anelastic properties by annealing can be also explained by both dislocation recovery and crack healing. Indeed, multiple micropores may represent a healed crack and would be connected under high stress. Therefore, it is difficult to separate the contributions from dislocations and microcracks. Further experiments under higher confining pressure are needed in order to assess the contribution from microcracks.

In addition, the removal of the deviatoric and confining stress and the slow quench performed before the anelasticity measurements might have inflicted some damage to the sample and/or sample-platen contact. In order to address this issue in future studies, we developed a new experimental system in which dislocation creep under confining pressure (0.8 MPa) and anelasticity measurement can be performed simultaneously. Preliminary results obtained recently using this new system show that Young's modulus (measured at 2 Hz) decreases gradually during dislocation creep. Although details will be reported elsewhere, this preliminary observation shows that the reduction of the Young's modulus after dislocation creep is not due to damage during unloading nor quench. Such in situ experiments will also enable us to investigate a possible effect of strain on anelasticity, which was not examined in this present study.

4.3. Comparison With Dislocation Damping

Although the dislocation creep-induced anelasticity obtained in this study cannot be attributed solely to a dislocation mechanism but might be affected by microcracks, it is, nonetheless, meaningful to compare this result to the dislocation damping observed in previous studies and examine whether the present anelasticity result can be understood as a dislocation mechanism.

We compare the present result with the previous knowledge on the dislocation-induced anelasticity in metallic crystals (e.g., Blanter et al., 2007; Nowick & Berry, 1972). Relaxation time scale of the dislocation effects in metals extends over a vast frequency range depending on the mechanism controlling the mobility of dislocation, as schematically illustrated in Figure 3.3.30 in Gremaud (2001). When pinned dislocation segments bow by glide without any interaction with other defects, the relaxation time scale is estimated as $B_v l^2 / 12\zeta$ with segment length l (m), dislocation energy ζ (J/m), and viscous drag coefficient B_v (Ns/m²), which is caused by the interaction of the moving dislocation with phonons (e.g., Blanter et al., 2007; Nowick & Berry, 1972). In metals, a dissipation peak caused by this mechanism exists at high frequencies (>10 MHz; Gremaud, 2001). In contrast, when the dislocation glide is rate-controlled by drag of point defects by diffusion, anelastic relaxation occurs at much lower frequencies (Gremaud, 2001). Because bowing of the dislocation segments without interaction with other defects does not involve diffusion (e.g., Kocks et al., 1975), a similar mechanism, if active in the borneol crystal, explains well the presence of the large peak at much higher frequency than the high-temperature background caused by the diffusion-controlled grain boundary sliding. Unlike metallic crystals, however, the peak did not reach the ultrasonic regime (~1 MHz). The above mentioned model suggests that borneol has larger B_v , larger l , and/or smaller ζ than metals, but so far, it is difficult to determine the reason for this discrepancy. In metallic crystals, the frequency and width of the peak(s) are known to depend on the crystal structure and height of Peierls potential (Karato & Spetzler, 1990; Nowick & Berry, 1972). With low Peierls potential, a simple string model works (e.g., Granato & Lüke K., 1956), but with high Peierls potential, kink motion has to be taken into account (e.g., Karato, 1998). Therefore, detailed knowledge of the borneol crystal will facilitate the understanding of the present result. To our knowledge, the crystal structure and Peierls potential of borneol (molecular crystal) have not been reported, although the high-temperature phase of borneol (≥ 72 °C at ambient pressure) is known as face-centered cubic (Sherwood, 1979).

We also compare the present result with the previous results of dislocation-induced anelasticity in olivine. The major results of Guéguen et al. (1989) and Farla et al. (2012) are summarized in Table 3. Guéguen et al. (1989) first reported a significant enhancement of attenuation in predeformed forsterite single crystals. They reported that the enhancement is more significant at lower frequencies and/or higher temperatures. Similar results were also reported by Farla et al. (2012). The dislocation-induced anelasticity captured by Farla et al. (2012) shows a frequency dependence similar to the high-temperature background caused by grain boundary sliding. Also, the deviation from the grain boundary effect was significant at high temperatures ($\geq 1,000$ °C). A similar result was found in an anelasticity study of polycrystalline ice that was actively

Table 3
Summary of Dislocation-Induced Anelasticity

	This study ^a	Farla et al. (2012)	Guéguen et al. (1989)	McCarthy and Cooper (2016)
Sample	Borneol PC	Olivine PC	Forsterite SC	Ice PC
f dependence	Peak	Broad absorption band	$Q^{-1} \propto f^{-0.21}$	Broad absorption band
ρ dependence	Yes	$Q^{-1} = 0.024 \times \rho^b$	Yes	—
T dependence	—	Yes	$Q^{-1} \propto e^{-H/R_g T c}$	Yes
Nonlinearity	—	No compelling evidence	(Probably)	Yes
Anisotropy	—	Yes	—	—

Note. PC = polycrystals; SC = single crystals.

^aContribution from microcracks might be included. ^b ρ is dislocation density in $(\mu\text{m})^{-2}$. Result of a 101-s period for compressively predeformed sample. ^c $H = 440$ kJ/mol.

deforming under high stress (McCarthy & Cooper, 2016). In this study, we could constrain well the frequency dependence of the dislocation creep-induced anelasticity. Unlike these previous studies, the obtained attenuation spectrum is a peak with a characteristic frequency much higher than those of the high-temperature background (Figure 12). Such a peak has not been reported in these previous studies. However, the possible existence of a peak at much higher frequency than the testing frequencies cannot be denied in these studies, because of a relatively large uncertainty in absolute value of the modulus measured from the forced oscillation tests; modulus data were not shown in Guéguen et al. (1989), were not analyzed quantitatively in McCarthy and Cooper (2016), and were discussed only tentatively in Farla et al. (2012). Because all relaxations existing at higher frequencies than seismic waves affect the wave velocity, the present approach using a rock analogue, for which Young's modulus can be measured accurately, can play a complementary role for the understanding of rock anelasticity.

5. Conclusions

Creep tests of polycrystalline borneol were conducted at $T = 40\text{--}50^\circ\text{C}$ with differential stress up to $\Delta\sigma \simeq 2$ MPa and confining pressure 0.8 MPa. The dominant deformation mechanism changes from diffusion to dislocation creep at $\Delta\sigma \simeq 2$ MPa. The stress exponent of steady-state dislocation creep was estimated as ~ 4 . Wavy grain boundaries were observed throughout the majority of the deformed samples, indicating the occurrence of dislocation-induced grain boundary migration, whereas microcracks were occasionally found, particularly near the outer cylindrical surface.

Effects of dislocation creep on anelasticity were captured by the forced oscillation test at $f < 100$ Hz as a significant reduction in Young's modulus and a slight increase in attenuation. In contrast, the Young's modulus measured at the ultrasonic frequency ($f = 1$ MHz) did not change. Therefore, a major part of the dislocation creep-induced anelastic relaxation is a peak with the characteristic frequency much higher than the major part of high-temperature background caused by grain-boundary sliding. These effects of prior high stress deformation mostly disappeared during the anelasticity measurements under low differential stress ($\Delta\sigma \simeq 0.28$ MPa). The recovery was thermally activated. Further experimental study under higher confining pressure is needed to assess the relative contribution from dislocations and microcracks to the observed changes in anelasticity.

Appendix A: Correction Factor for No-Slip Boundary Conditions

Let E_{app} be an apparent Young's modulus of a cylindrical sample (radius R and length L) measured by compressing the top and bottom surfaces with a rigid plane without slip. Here sample geometry is represented by aspect ratio $\alpha = R/L$. Let E_{true} be the true Young's modulus. Takei et al. (2014) defined correction factor γ as $E_{\text{true}} = \gamma E_{\text{app}}$, where γ depends on the Poisson's ratio ν and aspect ratio α of the sample. The correction factor used in this present study is explicitly written as

$$\frac{1}{\gamma} = a(\nu) \times \alpha + b(\nu), \quad (\text{A1})$$

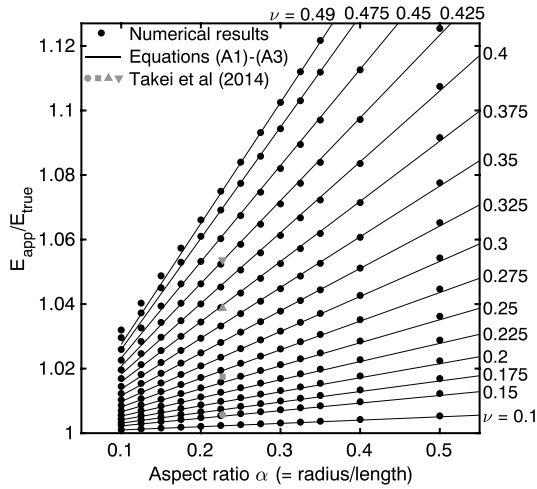


Figure A1. Apparent Young's modulus E_{app} divided by the true Young's modulus E_{true} versus sample aspect ratio α (=radius R /length L) for various Poisson's ratio ν . Black symbols show the numerical results, black lines show the approximation formula (A1)–(A3), and gray symbols at $\alpha = 0.227$ ($L/2R = 2.2$) show the factors used by Takei et al. (2014) for $\nu = 0.2$ (circle), 0.3 (square), 0.4 (triangle), and 0.45 (reverse triangle).

where $a(\nu)$ and $b(\nu)$ are given by

$$a(\nu) = 0.99314 \times \nu^2 + 2.3671 \times \nu^4, \quad (A2)$$

$$b(\nu) = 1 - 0.025144 \times \nu^3 - 0.50741 \times \nu^6. \quad (A3)$$

We obtained equations (A1)–(A3) as an approximation formula for the variation of E_{app}/E_{true} with α and ν numerically calculated by the finite element method described below (Figure A1). The difference between E_{app}/E_{true} from the numerical results and from equations (A1)–(A3) is within ± 0.002 for a range of $0.175 \leq \alpha \leq 0.4$ and $0 \leq \nu \leq 0.49$ or for a range of $0.1 \leq \alpha \leq 0.5$ and $0 \leq \nu \leq 0.425$. In this study, α was between 0.23 and 0.3, and ν was between 0.371 and 0.42 (the largest value of ν occurs at the highest temperature and lowest frequency). The γ^{-1} accurately determined in this study is slightly (<0.008) larger than the previous one used by Takei et al. (2014; gray symbols in Figure A1).

The finite element method was used to solve the axisymmetric equations of linear elasticity in a cylinder of radius R and height L . Owing to mirror symmetry, it is sufficient to solve the equations just for the top half of the cylinder. The boundary conditions are

$$\sigma_{rr}, \sigma_{rz} = 0 \quad \text{on} \quad r = R, \quad (A4)$$

$$u_r = 0 \quad \text{on} \quad z = L/2, \quad (A5)$$

$$u_z = \epsilon_0 L/2 \quad \text{on} \quad z = L/2, \quad (A6)$$

$$u_z, \sigma_{rz} = 0 \quad \text{on} \quad z = 0, \quad (A7)$$

where ϵ_0 is the imposed strain, \mathbf{u} is the displacement, and σ is the stress tensor. Equation (A4) imposes zero traction on the curved sides of the cylinder. Equations (A5) and (A6) prescribe the displacement at the ends of the cylinder, which is bonded such that there is zero radial displacement. Equation (A7) imposes mirror symmetry about the cylinder midplane. The apparent Young's modulus can be determined from the volume average of σ_{zz}

$$E_{app} = \frac{1}{\epsilon_0 V} \int_V \sigma_{zz} dV, \quad (A8)$$

where V is the volume. The governing equations were discretized using the FEniCS software (Logg & Wells, 2010; Logg et al., 2012). Cubic triangular Lagrange elements were used to represent the displacement \mathbf{u} . Mesh points were evenly spaced with N_r points in the radial direction and N_z in the vertical, where

$$N_r = \max(N, RN/L), \quad (A9)$$

$$N_z = \max(N/2, LN/2R), \quad (A10)$$

and $N = 128$, to ensure an equal spacing of grid points in both directions.

References

- Blanter, M. S., Golovin, I. S., Neuhäuser, H., & Sinning, H.-R. (2007). *Internal friction in metallic materials: A handbook*. Berlin: Springer-Verlag.
- Chopra, P. N. (1997). High-temperature transient creep in olivine rocks. *Tectonophysics*, 279, 93–111. [https://doi.org/10.1016/S0040-1951\(97\)00134-0](https://doi.org/10.1016/S0040-1951(97)00134-0)
- Cooper, R. F. (2002). Seismic wave attenuation: Energy dissipation in viscoelastic crystalline solids. *Reviews in Mineralogy and Geochemistry*, 51(1), 253–290. <https://doi.org/10.2138/gsrmg.51.1.253>
- Cooper, R. F., Stone, D. S., & Ploekphol, T. (2016). Load relaxation of olivine single crystals. *Journal of Geophysical Research: Solid Earth*, 121, 7193–7210. <https://doi.org/10.1002/2016JB013425>
- D'Ans, J., Jänchen, D., Kaufmann, E., & Kux, C. (1964). *Landolt-Börnstein Zahlenwerte und Funktionen aus Physik, Chemie, Astronomie, Geophysik, und Technik, II-2c, Lösungsgleichgewichte II*. Berlin: Springer-Verlag.

Acknowledgments

The authors would like to thank Ayako Suzuki for helpful discussions and experimental supports, M. Uchida for technical assistance, and A. Yasuda for allowing us to access the microscope. L. Hansen and an anonymous referee provided thoughtful reviews, which greatly improved this paper. This work was supported by JSPS KAKENHI grant JP15K13560. ERI International Office supported the visit of C. M. Experimental data set of this study can be accessed online (http://www.eri.u-tokyo.ac.jp/people/ytakei/Sasaki_etal_JGR2019/).

- Evans, B., Fredrich, J., & Wong, T.-F. (2016). The brittle-ductile transition in rocks: Recent experimental and theoretical progress. In A. G. Duba, W. B. Durham, J. W. Handin, & H. F. Wang (Eds.), *The brittle-ductile transition in rocks*, *Geophys. Monogr.* (Vol. 56, pp. 1–20). USA: AGU publications. <https://doi.org/10.1029/GM056p0001>
- Farla, R. J. M., Jackson, I., Fitz Gerald, J. D., Faul, U. H., & Zimmerman, M. E. (2012). Dislocation damping and anisotropic seismic wave attenuation in Earth's upper mantle. *Science*, 6079, 332–335. <http://science.sciencemag.org/content/336/6079/332.abstract>
- Granato, A. V., & Lücke, K. (1956). Theory of mechanical damping due to dislocation. *Journal of Applied Physics*, 27, 583–593. <https://doi.org/10.1063/1.1722436>
- Gremaud, G. (2001). Dislocation-point defect interactions. In R. Schaller, G. Fantozzi, & G. Gremaud (Eds.), *Mechanical spectroscopy Q^{-1} 2001 with applications to materials science* (pp. 178–246). Zurich: Trans Tech Publications.
- Gribb, T. T., & Cooper, R. F. (1998). Low-frequency shear attenuation in polycrystalline olivine: Grain boundary diffusion and the physical significance of the Andrade model for viscoelastic rheology. *Journal of Geophysical Research*, 103(B11), 27,267–27,279. <https://doi.org/10.1029/98JB02786>
- Guéguen, Y., Darot, M., Mazot, P., & Woïrgard, J. (1989). Q^{-1} of forsterite single crystals. *Physics of the Earth and Planetary Interiors*, 55(3–4), 254–258. [https://doi.org/10.1016/0031-9201\(89\)90073-3](https://doi.org/10.1016/0031-9201(89)90073-3)
- Hansen, L. N., Zimmerman, M. E., & Kohlstedt, D. L. (2012). The influence of microstructure on deformation of olivine in the grain-boundary sliding regime. *Journal of Geophysical Research*, 117, B09201. <https://doi.org/10.1029/2012JB009305>
- Hanson, D. R., & Spetzler, H. A. (1994). Transient creep in natural and synthetic, iron-bearing olivine single crystals: Mechanical results and dislocation microstructures. *Tectonophysics*, 235, 293–315. [https://doi.org/10.1016/0040-1951\(94\)90191-0](https://doi.org/10.1016/0040-1951(94)90191-0)
- Jackson, I., & Faul, U. H. (2010). Grain-size-sensitive viscoelastic relaxation in olivine: Towards a robust laboratory-based model for seismological application. *Physics of the Earth and Planetary Interiors*, 183(1–2), 151–163. <https://doi.org/10.1016/J.PEPI.2010.09.005>
- Jackson, I., Faul, U. H., Fitz Gerald, J. D., & Tan, B. H. (2004). Shear wave attenuation and dispersion in melt-bearing olivine polycrystals: 1. Specimen fabrication and mechanical testing. *Journal of Geophysical Research*, 109, B06201. <https://doi.org/10.1029/2003JB002406>
- Jackson, I., Faul, U. H., & Skelton, R. (2014). Elastically accommodated grain-boundary sliding: New insights from experiment and modeling. *Physics of the Earth and Planetary Interiors*, 228, 203–210. <https://doi.org/10.1016/J.PEPI.2013.11.014>
- Jackson, I., Fitz Gerald, J. D., Faul, U. H., & Tan, B. H. (2002). Grain-size-sensitive seismic wave attenuation in polycrystalline olivine. *Journal of Geophysical Research*, 107(B12), 2360. <https://doi.org/10.1029/2001JB001225>
- Karato, S. (1998). A dislocation model of seismic wave attenuation and micro-creep in the Earth: Harold Jeffreys and the rheology of the solid Earth. *Pure and Applied Geophysics*, 153, 239–256. <https://doi.org/10.1007/s000240050195>
- Karato, S., & Spetzler, H. A. (1990). Defect microdynamics in minerals and solid-state mechanisms of seismic wave attenuation and velocity dispersion in the mantle. *Reviews of Geophysics*, 28(4), 399–421. <https://doi.org/10.1029/RG028i004p00399>
- Kocks, U. F., Argon, A. S., & Ashby, M. F. (1975). *Thermodynamics and kinetics of slip*. Oxford: Pergamon press.
- Kohlstedt, D. L., & Goetze, C. (1974). Low-stress high-temperature creep in olivine single crystals. *Journal of Geophysical Research*, 79(14), 2045–2051. <https://doi.org/10.1029/JB079i014p02045>
- Logg, A., Mardal, K.-A., & Wells, G. (2012). *Automated solution of differential equations by the finite element method, Lecture notes in computational science and engineering vol 84*. Berlin Heidelberg: Springer. <https://link.springer.com/book/10.1007/978-3-642-23099-8>
- Logg, A., & Wells, G. N. (2010). DOLFIN: Automated finite element computing. *ACM Transactions on Mathematical Software*, 37(2), 20. <http://doi.acm.org/10.1145/1731022.1731030>
- McCarthy, C., & Cooper, R. F. (2016). Tidal dissipation in creeping ice and the thermal evolution of Europa. *Earth and Planetary Science Letters*, 443, 185–194. <https://doi.org/10.1016/j.epsl.2016.03.006>
- McCarthy, C., & Takei, Y. (2011). Anelasticity and viscosity of partially molten rock analogue: Toward seismic detection of small quantities of melt. *Geophysical Research Letters*, 38, L18306. <https://doi.org/10.1029/2011GL048776>
- McCarthy, C., Takei, Y., & Hiraga, T. (2011). Experimental study of attenuation and dispersion over a broad frequency range: 2. The universal scaling of polycrystalline materials. *Journal of Geophysical Research*, 116, B09207. <https://doi.org/10.1029/2011JB008384>
- Mei, S., & Kohlstedt, D. L. (2000). Influence of water on plastic deformation of olivine aggregates 2. Dislocation creep regime. *Journal of Geophysical Research*, 105(9), 21,471–21,481. <https://doi.org/10.1029/2000JB900180>
- Morris, S., & Jackson, I. (2009). Diffusionally assisted grain-boundary sliding and viscoelasticity of polycrystals. *Journal of the Mechanics and Physics of Solids*, 57(4), 744–761. <https://doi.org/10.1016/J.JMPS.2008.12.006>
- Nowick, A. S., & Berry, B. S. (1972). *Anelastic relaxation in crystalline solids*. San Diego: Academic Press.
- O'Connell, R. J., & Budiansky, B. (1974). Seismic velocities in dry and saturated cracked solids. *Journal of Geophysical Research*, 79, 5412–5426. <https://doi.org/10.1029/JB079i035p05412>
- Raj, R. (1975). Transient behavior of diffusion-induced creep and creep rupture. *Metallurgical Transactions A*, 6(8), 1499–1509. <https://doi.org/10.1007/BF02641961>
- Sherwood, J. N. (1979). Lattice defects, self-diffusion, and the plasticity of plastic crystals. In J. N. Sherwood (Ed.), *The plastically crystalline state: Orientationally disordered crystals* (pp. 39–83). New York: Wiley Intersci.
- Takei, Y. (2000). Acoustic properties of partially molten media studied on a simple binary system with a controllable dihedral angle. *Journal of Geophysical Research*, 105(B7), 16,665–16,682. <https://doi.org/10.1029/2000JB900124>
- Takei, Y. (2017). Effects of partial melting on seismic velocity and attenuation: A new insight from experiments. *Annual Review of Earth and Planetary Sciences*, 45, 447–470. <https://www.annualreviews.org/doi/10.1146/annurev-earth-063016-015820>
- Takei, Y., Karasawa, F., & Yamauchi, H. (2014). Temperature, grain size, and chemical controls on polycrystal anelasticity over a broad frequency range extending into the seismic range. *Journal of Geophysical Research: Solid Earth*, 119, 5414–5443. <https://doi.org/10.1002/2014JB011146>
- Tatsuoka, F. (1988). Some recent developments in triaxial systems for cohesionless soils. In R. T. Donaghe, R. C. Chaney, & M. L. Silver (Eds.), *Adv. Triaxial Test. Soil Rock* (Vol. STP 977, pp. 7–67). Philadelphia: ASTM. <https://doi.org/10.1520/STP29068S>
- Toriumi, M., & Karato, S. (1978). Experimental studies on the recovery process of deformed olivines and the mechanical state of the upper mantle. *Tectonophysics*, 49, 79–95. [https://doi.org/10.1016/0040-1951\(78\)90098-7](https://doi.org/10.1016/0040-1951(78)90098-7)
- Underwood, E. E. (1970). *Quantitative stereology*. Boston, MA: Addison-Wesley Pub. Co.
- Yamauchi, H., & Takei, Y. (2016). Polycrystal anelasticity at near-solidus temperatures. *Journal of Geophysical Research: Solid Earth*, 121, 7790–7820. <https://doi.org/10.1002/2016JB013316>